Electronic Supplementary Material (ESI) for Sustainable Energy & Fuels.

Supplementary information

Resistance-based analysis of limiting interfaces in multilayer water splitting photocathodes by impedance spectroscopy

*Thomas Moehl, Wei Cui, René Wick-Joliat, S. David Tilley**

Department of Chemistry, University of Zurich, Winterthurerstrasse 190, CH-8057 Zurich

*E-mail: david.tilley@chem.uzh.ch.

Experimental part

Device fabrication

Growth of polycrystalline Cu_2O substrate by thermal oxidation: High-purity Cu foil (Jiarun Material, 99.9999%) with a thickness of 0.05 mm was oxidized following the method of Minami.[1,2] The Cu foil was cut into small pieces of about 15 mm*15 mm. The Cu substrates were heated in a quartz tube furnace under argon from room temperature to 1030ºC over 1 hour and kept for 1 hour at this temperature. Afterwards, air was introduced into the tube and the foils were oxidized at 1030 ºC for 2 hours. Argon was again introduced into the tube and the sheets were further annealed at 1030 ºC for 2 hours. Finally, the temperature was reduced to 500 ºC in 1 hour and then allowed to cool naturally to room temperature under argon. The final thickness of the Cu_2O film is 75 μm.[3]

Atomic layer deposition of Ga_2O_3 and TiO_2 layers: The Ga_2O_3 and TiO_2 layers were deposited on the Cu_2O substrate using a thermal ALD system (PICOSUN, R-200). The Ga_2O_3 film was deposited at a reactor temperature of 160 °C using bis(μ-dimethylamino)tetrakis(dimethylamino)digallium (STREM, 98%) and

H_2O as the Ga and O sources. The TiO_2 film was deposited at a reactor temperature of 120°C with tetrakis(dimethylamino)titanium (Aldrich, 99.99%) and H_2O as the precursors of Ti and O. The temperature of the Ga, Ti, and O precursor cylinders were held at 150 °C, 85 °C and room temperature, respectively. A "boost" sequence was used for the Ga and Ti precursor cylinders, whereby nitrogen gas was introduced into the cylinder following each pulse, by increasing the line pressure while the valve to the precursor remained open. This increases the pressure inside the precursor bottle and prepare the release of the precursor for the next cycle of ALD deposition. For Ga_2O_3, the Ga precursor valve was opened for 2.5 s (0.5 s dosing to the reactor, 2.1 s of increased line pressure), followed by a 7.0 s N_2 purge. Then a 0.1 s pulse of H_2O was used, followed by a 4.0 s N_2 purge. For TiO_2, the Ti precursor ALD valve was opened for 1.6 s (0.5 s dosing to the reactor, 1.2 s of increased line pressure), followed by a 6.0 s N_2 purge. Then a 0.1 s pulse of H_2O was used, followed by a 6.0 s N_2 purge. For a more detailed description of the ALD machine and the deposition process please refer to Moehl et al.[4] The ALD Ga_2O_3 layers used for the MS plots were directly deposited on ITO (Cleaning: mechanically with soap (deconex 0.5 vol% in Milli-Q water) and afterwards sequentially in acetone, water, and ethanol (ultrasonic bath, 10 min each step).

Fabrication of the Cu_2O photocathodes: For the TO-Cu_2O photocathode, a 100 nm gold layer was deposited by sputtering onto the backside of the Cu_2O sheet to form an ohmic contact with the p-type semiconductor. A copper wire was connected to the gold layer with silver paste. The Cu_2O sheet was masked and fixed by opaque epoxy on microscopy glass slides, exposing only the copper wire and part of the TiO_2 layer (the active area). A more detailed description of the device fabrication can be found by Niu et al.[3] For the etching of the cuprous oxide following procedure was applied: The as-prepared Cu_2O foils was immersed in a diluted nitric acid (1:1 of H_2O and 65% HNO_3) for 10 seconds, followed by rinsed with DI water and sonicated in isopropanol for 30 seconds. Finally the foils was dried under Nitrogen flow and immediately transferred into the ALD chamber.

Preparation of the pSi photocathodes: p-Si wafers were bought from Siltronix, (Boron doping, 10-30 ohm cm, single side polished) and cut into 1x1cm pieces, which were then cleaned by ultrasonicating for 10 min each in acetone, soapy water (Deconex), water and ethanol, followed by 10 min at 50 °C in $H_2O/H_2O_2/NH_4OH$ (5:1:1) solution and 30 s in 2% HF solution at room temperature. Samples were then rinsed with water, dried in N_2 stream and immediately used for the ALD TiO2 deposition.

RuO_x *catalyst deposition:* Ruthenium oxide (RuO_x) was used as the HER catalyst in our photocathode to get a stable water splitting performance. The RuO_x was photoelectrodeposited under 1 sun illumination with a constant current density of -28.3 µA cm^{-2} from a 1.3 mM potassium perruthenate ($KRuO_4$, Alfa Aesar) solution, as described in the literature.[5] For the Cu_2O the deposition time was 15 mins yielding a deposited charge of 0.0255 C cm^{-2}. Previous work has shown that this deposition procedure results in a hydrous, amorphous RuO_x layer approximately 40 nm thick.[5]

Experimental information

(Photo)electrochemical Measurements: PEC performance of the Cu_2O photocathodes was carried out in a three-electrode electrochemical cell. A potentiostat (BioLogic SP-300) was used to control the potential of the working electrode. A Pt wire and an Ag/AgCl electrode (KOSLOW, saturated KCl, +0.197 V *vs.* SHE) were used as counter and reference electrode, respectively. The electrolyte used in all PEC measurements was prepared by dissolving 0.5 M $NaSO_4$ (Sigma Aldrich) and 0.1 M KH_2PO_4 (Sigma Aldrich) in deionized water (18.2 MΩ cm) and adjusting the pH to 5 with 2 M KOH solution. For measurements under illumination a white light bias by LEDs (SP-12-W5, cool white Luxeon Rebel) of 10 % was used (if not stated otherwise). We have normally used 10% of a sun as light intensity for our investigations as especially in PEC the

formation of gas bubbles and their release can lead to deterioration of the acquired EIS data (we also added TritonX to the electrolyte solution to minimize the size of the bubbles formed (1mM)). The light intensity was calibrated with a calibrated silicon diode (8 mm diameter) with a BK7 window from PV Measurements, Inc (PVM558). Due to the large mismatch of the spectra of the white LEDs and Xenon lamp with AM 1.5 G filter, the percentage of "10% sun" is only approximate. All potentials in this paper were converted into RHE scale using Equation ($V_{RHE} = V_{Ag/AgCl} + 0.059 \times pH + 0.197\ V$). If not mentioned otherwise standard devices are presented in the Figures (p-Si/100 nm TiO_2/RuO_x and Cu_2O/20 nm Ga_2O_3/100 nm TiO_2/RuO_x).

Electrochemical impedance measurements: For the direct comparison we have used samples from the same batch of Cu_2O synthesis to exclude batch to batch variation which could distort the conclusions. Electrochemical impedance measurements were performed with a BioLogic SP-300. Before each EIS measurement a preconditioning of the device at the starting potential of 180 s was implemented to achieve the steady state of the RuO_x/ electrolyte solution interface. The bias potential steps were between 30 and 50 mV and the equilibration time at each bias potential step was normally 29s. The frequency range used was 1 MHz to 0.2 Hz. For measurements under illumination a white light bias of 10% sun was normally used (see photoelectrochemical experiments). The EIS spectra were fitted with Zview from Scribner. On the model used for the fitting procedure please see below. The direct comparisons between the different thicknesses of TiO_2 and Ga_2O_3 as well as the etching treatment were conducted with samples made in the same batch to exclude sample to sample variation. The current voltage curves (in the dark and under illumination) presented in this manuscript are extracted from DC current values during the EIS measurements. To extract these values from the EIS measurements we used the current values from the lowest frequency, which represents a stabilization for the DC current of roughly 70 s (stabilization time plus measurement time).

Photocurrent transient measurements: For the white light measurements, an array of nine white light diodes was used (SP-12-W5, cool white Luxeon Rebel) controlled by a Keithley power source (PSW4323). A Keithley sourcemeter (Model: 2602B) was used to control the voltage of the PEC cell and record the current. Igor Pro (vers. 7) was used to control the complete measurement setup. The transient photocurrent measurements were performed at 10% white light bias. with an additional Keithley power source (PSW4323) that controlled an array of four colored LEDs (λ_{blue}=447 nm (SP-12-V4); λ_{red}=627nm (SP-12-R5); λ_{green}=530nm (SP-12-G4); Luxeon Rebel). A fast solid-state switch was used to ensure a fast rise and decay of the colored LEDs (a squared pulse with 100 ns rise and fall time). A white light bias was used for the photocurrent transient measurements. The light intensity was calibrated with an NREL calibrated silicon diode (8 mm diameter) with a BK7 window from PV Measurements, Inc (PVM558). Light intensities used for the light pulses were 5 to 10% of a sun (i.e. 50 to 100 % of the steady state white light bias).

Consideration of possible photophysical and -electrochemical processes

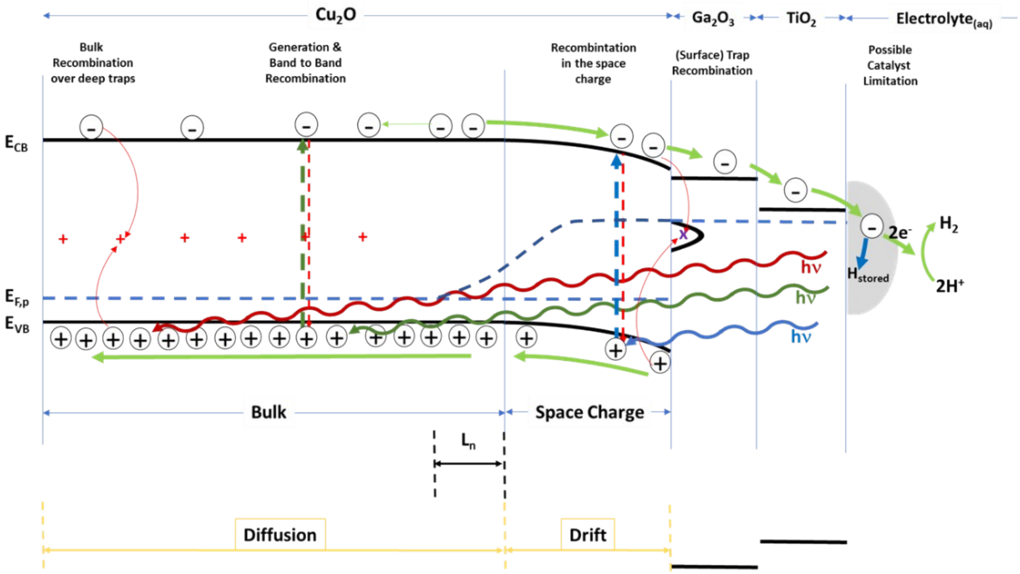

Fig. S 1 Idealised scheme of the photophysical and electrochemical processes in Cu_2O devices.

In Fig. S 1 we have drawn a simplified picture of the Cu_2O devices and most common photophysical and electrochemical processes which could possibly take place in a multilayer photocathode device. Not necessarily all the processes can be observed or exist, e.g. the filling and release of charge carriers from deep traps in Cu_2O is a very slow process in the range of minutes. [6]

Generally, we can assume that the photogenerated charge carriers are, after generation, subjected to a recombination process inside the space charge region of the photoabsorber (or at the build in junction). This process normally takes place in the µs range for sufficiently efficient devices and is therefore situated in the HF region of the EIS measurements (MHz down to kHz). In stronger depletion of the p-type semiconductor the recombination resistance associated to the process should increase as the recombination current is suppressed by the increased band bending at the contact to the n-type material. Before the recombination can be suppressed by the stronger band bending the resistance associated is normally constant as it is dominated by the recombination process associated to the bulk of the photoabsorber. A good overview on the investigated systems can be found in Cui et al. describing and measuring the build in voltage and the surface potential to the electrolyte solution of PEC photoelectrodes.[7] A slow process (ms to s) will be the electron charge transfer into the electrolyte, generating Hydrogen and is normally represented by R_{ct}. Latter resistance relates to the current from the catalyst to the electrolyte solution and therefore the kinetic step for hydrogen formation and mirrors the actual H_2 generating photocurrent. In EIS measurements this process will appear in the mHz to Hz range. The RuO_x catalyst will absorb and reduce a proton during its first reduction step and will form an equilibrium with the surrounding electrolyte solution. Processes related to intercalation reaction e.g. into metal oxides can take place at time scales of seconds. [8,9]

Resistance-based EIS analysis

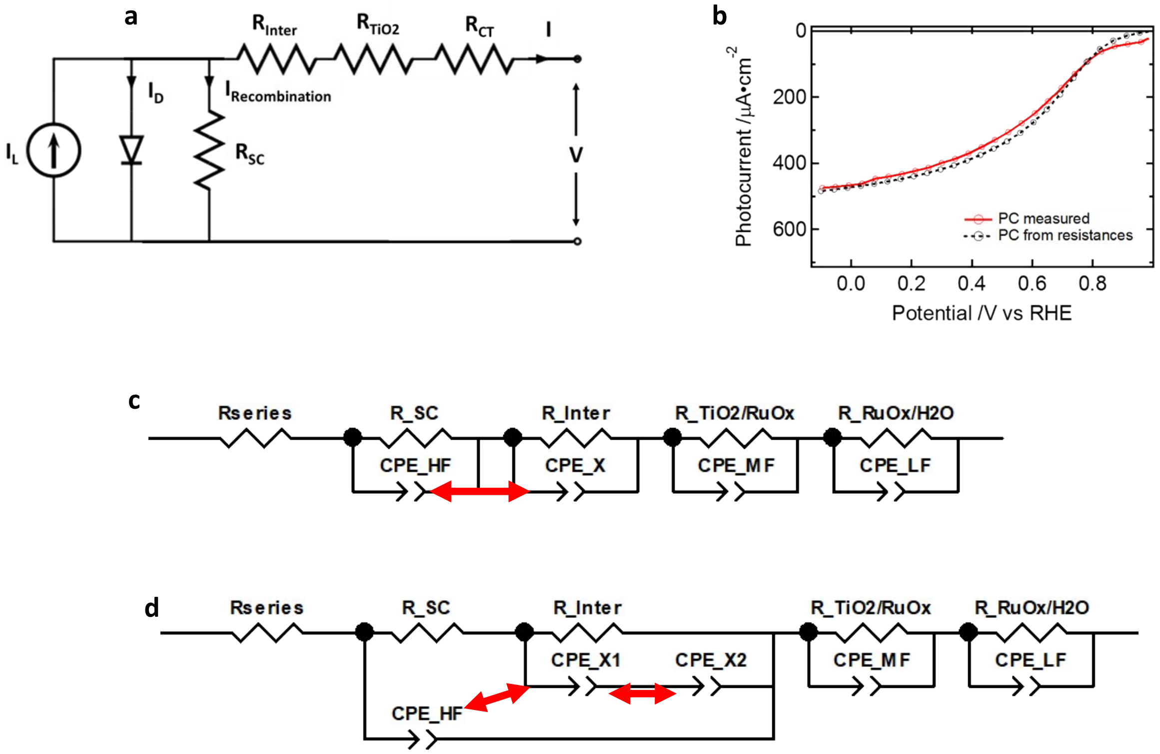

Fig. S 2 (a) Circuit model of a PEC cell with I_L as photogenerated current, I_D as dark current of the diode, $I_{recombination}$ as recombination current of photogenerated charge and I as overall current; (b) photocurrent regeneration from the determined resistances of the EIS fitting of Cu_2O-based device at 5% sun; (c) equivalent circuit model used to fit the Cu_2O devices, (d) possible variation of the capacitances, but with similar resistive contribution.

The EIS spectra under illumination showed a maximum of three different processes for silicon, and four process for the Cu_2O photocathodes. In Fig. S 2 a) the equivalent circuit model without capacitances of PEC device is presented. As visible all the resistances are in series. If resistances are in parallel, the lower resistance dominates the overall resistance as charge carriers flow through the less resistive way ($1/R_{sum}=(1/(R_{small})+1/(R_{high})$ with $R_{small} << R_{high} \sim R_{sum}=R_{small}$). If one of the two parallel resistances is 10 times smaller as compared to the other one, the error due to the higher resistance in parallel is 10%.

The overall DC resistance (the sum of all determined resistances during the fitting procedure $R_{Total} = \sum R_{\text{Determined}}$) can be used to validate the result by a regeneration of the actual JV curve ($I = \int \frac{1}{R_{Total}} dV$) as represented in Fig. S 2b.

The EI spectra were fitted with simple resistive and capacitive elements in parallel (RC), which were then connected in series depending on how many processes were observed in the Nyquist plot, Fig. S 2c. To account for non-ideality of the capacitors constant phase elements, CPEs, have been used (with the exponent accounting for the ideality of the CPE not going below 0.8). This approach of fitting the data yields a reduced picture of the photophysical processes. However, the determined resistances and their dependence on the applied potential still enable one to draw valuable conclusions on the operation of the system and the assigning of the resistances to a certain photophysical or electrochemical process.

An evaluation of determined capacitances is not straight forward due to the limited methods for cross-checking the actual results.

In the case of the capacitances, such a rough evaluation like in the case of the resistances would be much more difficult.

- The actual number of capacitive contributions is unknown as well as the overall capacitance of the system. Therefore, one cannot cross-check the determined capacitance values by regeneration of the JV curve like in the case of the resistances (Fig. S 2b).
- The EC models in Fig. S 2c and d would lead to very similar resistive contributions but different time constants of the associated processes of R_{SC} and R_{Inter}.
- If capacitances are in parallel, they add up and one cannot access each single contribution of this sum (see e.g. Fig. S 2d and Fig. 1).
- The capacitances of the space charges of e.g. buffer and protection layer are present at both sides of the layer (and might differ due to the different contacting materials; see Fig. S 2d). This would represent two capacitances in series which are in the same range of values and therefore separating them during the fitting procedure can lead to instable fitting of the data.
- As the EIS spectra are complex, the stability of the EIS fitting procedure (at each potential) itself can vary and lead to strong variations of the results, especially of the determined capacitances.

As we do not have direct access to the capacitances, we cannot determine the time (or rate) constants for the related processes.

Tab. S 1 Frequency regions of the detected resistances under illumination

Photoabsorber	**Resistance (related process or interface)**	**Frequency Range**
p-Silicon	R_{sc} (recombination inside the semiconductor junction)	100 kHz-1 kHz
	R_{TiO2} (potential barriers at the TiO_2/ electrolyte solution)	1 kHz-mHz
	R_{CT} (charge transfer resistance to the electrolyte solution or catalyst reduction)	10 Hz-mHz
Cu_2O	R_{sc}	100 kHz-10 kHz
	R_{Inter} (resistance unique to the Cu_2O; set together out of two resistances; determining the FF in region III ($R_{Surface}$), presenting the potential barrier at the Ga_2O_3/ TiO_2 interface (R_{Ga}))	10 kHz-10 Hz
	R_{TiO2}	10 kHz-mHz
	R_{CT}	10Hz-mHz

Mott-Schottky plots

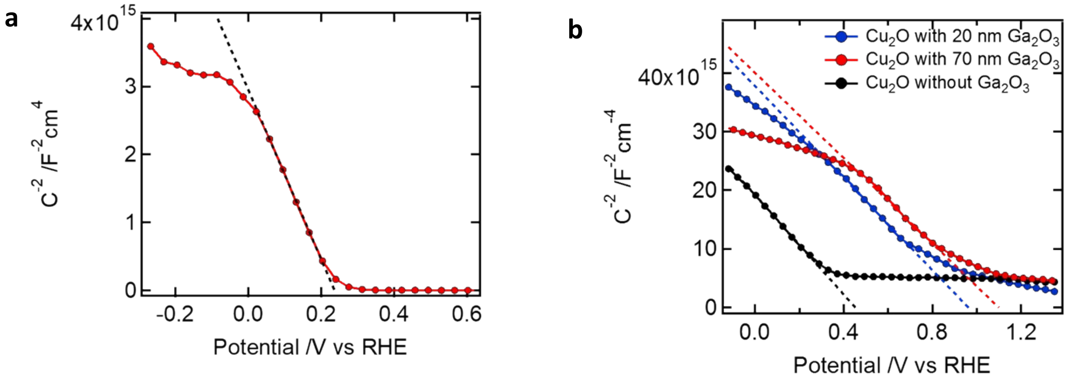

Fig. S 3 (a) MS plot of a standard silicon device; (b) MS plots of the Cu_2O devices in Fig. 6 of the main manuscript (with varying ALD Ga_2O_3 thickness and 100 nm ALD TiO_2 and RuO_x).

Under dark conditions no minority carriers (electrons in case of a p-type semiconductor) are present in depletion region of a semiconductor. The potential perturbation during an EIS measurement is therefore determined by the majority carriers. In the adequate frequency range, the space charge capacitance of the semiconductor, C_{sc}, can be probed. In our measurements we have extracted C_{sc} from the high frequency semicircle of the Nyquist plots (kHz range) without fitting the low frequency component. In contrast to a “normal” Mott-Schottky (MS) analysis, which is usually performed only at one frequency, in EIS analysis no frequency dispersion appears when extracting C_{sc} as one determines directly the space charge capacitance at each potential by the fitting procedure. The space charge capacitance is then plotted as $1/C_{sc}^2$ vs the applied potential (see e.g. Fig. S3 and 4), to determine the flat band potential from a linear extrapolation to the x axis (x axis intercept). The slope of the fit is proportional to the doping density:

$$\frac{1}{C_{SC}^2} = \frac{2}{N_D \varepsilon \varepsilon_0 q}\left(E - E_{FB} - \frac{kT}{q}\right)$$

where q is the charge of an electron, ε is the relative dielectric constant of the materials, ε_0 is the permittivity of free space, N_D donor density (for an n-type semiconductor), E is the potential applied, E_{FB} is the flat band potential, k is the Boltzmann constant and T is the temperature.

The E_{FB} obtained by this method represents the position of the Fermi level of the lowest doped semiconductor. To access the final position of the conduction or valence band the E_{FB} distance to the conduction or valence band position can be calculated by:

$$E_{CB} - E_{FB} = \frac{kT}{q}\ln\left(\frac{N_C}{N_D}\right)$$

where N_C is the number of available states in the conduction band. In Fig. S3 we can observe the results from the MS plots of the Cu_2O- and Si-based devices. The values used for the calculation are in Table S 2.

The slopes show as expected p-type behavior for the Si and the Cu_2O. In case of the Si a doping density of 3e15 cm^{-3} is found and is therefore in the expected range of specification of the wafer (1-30 Ohm cm^2). The E_{FB} potential is at 240 mV vs RHE. For the Cu_2O the MS plots yielded a doping densities between 1-5e14 cm^{-3} in accordance with the results from Hall measurements.[3] The E_{FB} of the Cu_2O standard devices were in the range of 800 to 950 mV vs RHE.

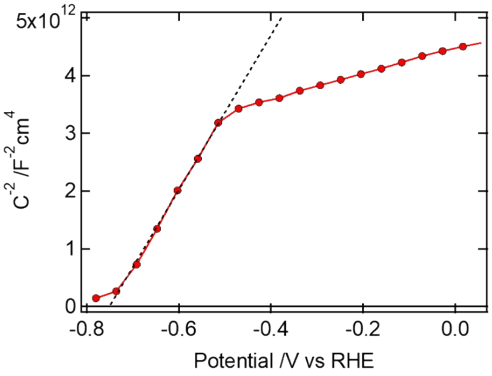

Fig. S 4 MS plot of 40 nm ALD Ga_2O_3 on ITO measured in pH 10 (KOH).

To implement the band positions of Ga_2O_3, ALD layers of the metal oxide were deposited on ITO and investigated by MS analysis. The doping determined was about 9e17 cm^{-3} yielding a conduction band position of about -850 mV (Fig. S 4).

The band positions of the ALD deposited TiO_2 have been investigated[4] in detail showing the E_{CB} edge to be at -50 to -100 mV vs RHE for the layer thicknesses used. Implementing this information into a scheme of the energetic positions, a barrier at the TiO_2 catalyst interface can be observed.

To draw the band diagrams presented in Figure 1 of the main manuscript we have applied Anderson's rule.[10]

The information on energetic position of the band edges originate from complete devices (Cu_2O and pSi) but also from the single layer MS analysis (here ITO/Ga_2O_3 and FTO/TiO_2). One must be aware that such band diagrams can give a good indication on the energetic situation of your system but special interface features like e.g. surface states or interface dipoles are neglected.

Tab. S 2 Data used for the calculations and results of the MS plots

Material	**ε**	**Nc 10^{19} cm^{-3}**	**N_d or N_a cm^{-3}**	**E_{FB} vs RHE mV**	**ΔE_{CB} mV**	**ΔE_{VB} mV**
p-Si	11	1	1-3e15	200 to 240	~150	
p-Cu_2O (with 20 nm Ga_2O_3 interlayer)	7.6 ([3])	1.1	1-5e14	800 to 950		~250
n-Ga_2O_3	10 ([11])	1	9e17	-770	~80	

Properties of the RuO_x catalyst

We have investigated the RuO_x hydrogen evolution catalyst deposited on ITO to better understand its electrochemical properties by EIS. The EC used was a simple RC element with an additional resistance accounting for the series resistance (Fig. S 5). The RC element represents the charge transfer into the electrolyte and the constant phase element the capacitance inside the catalyst and at the interface to the electrolyte solution.

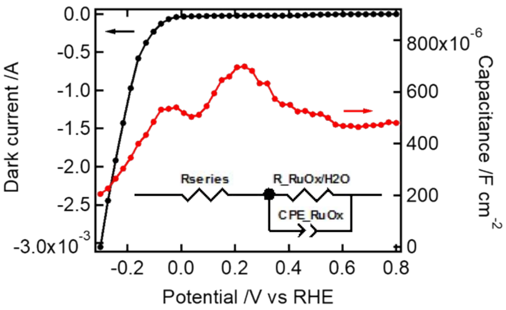

Fig. S 5 Dark current and the capacitance of the RuO_x/ electrolyte solution interface; Inset: EC model used for the fitting of the EIS data

The Ru(IV)O_x catalyst has to be reduced twice, first from Ru(IV) to Ru(III) and then to Ru(II), to be catalytically active for hydrogen evolution. The latter two reduced states are labeled $RuO_x{}^{1-}$ and $RuO_x{}^{2-}$. The redox chemistry of Ru(IV)O_x has been discussed in the literature by several groups, though the actual nature of the catalytically active species is still uncertain.[12–17] Generally, it is assumed that the hydrogen evolution reaction involves ruthenium hydroxy species at the surface of the catalyst layer.[15] Doblhofer et al. showed that the reduction of Ru(IV) to Ru(III) takes place for potentials lower than 0.4 V vs RHE and the reduction to Ru(II) from 0.1 V vs RHE on.[13,17] Pastor et al. have shown the formation of the $RuO_x{}^{1-}$ and $RuO_x{}^{2-}$ by transient absorption spectroscopy by detecting the absorption change in the catalyst due to the change of redox state.[12] The authors show an increase of the $RuO_x{}^{1-}$ signal from 0.8 V vs RHE on with a maximum at ~0.1 V vs RHE and the formation of $RuO_x{}^{2-}$ from 0 V vs RHE on.

For our electrodes we measured an increase of the capacitance from 0.6 V vs RHE with a maximum at ~0.25 V vs RHE after which it reduces (Fig. S 5). At about 0.1 V vs RHE it increases again as the formation of $RuO_x{}^{2-}$ sets in. Using the difference of the maxima in accumulated charge from the photocurrent transients in Fig. 5, the redox potential difference between $RuO_x{}^{1-}$ and $RuO_x{}^{2-}$ is estimated to be 0.4 to 0.5 V, which was then implemented into Fig. 1.

Nyquist and Bode plots of the devices under illumination

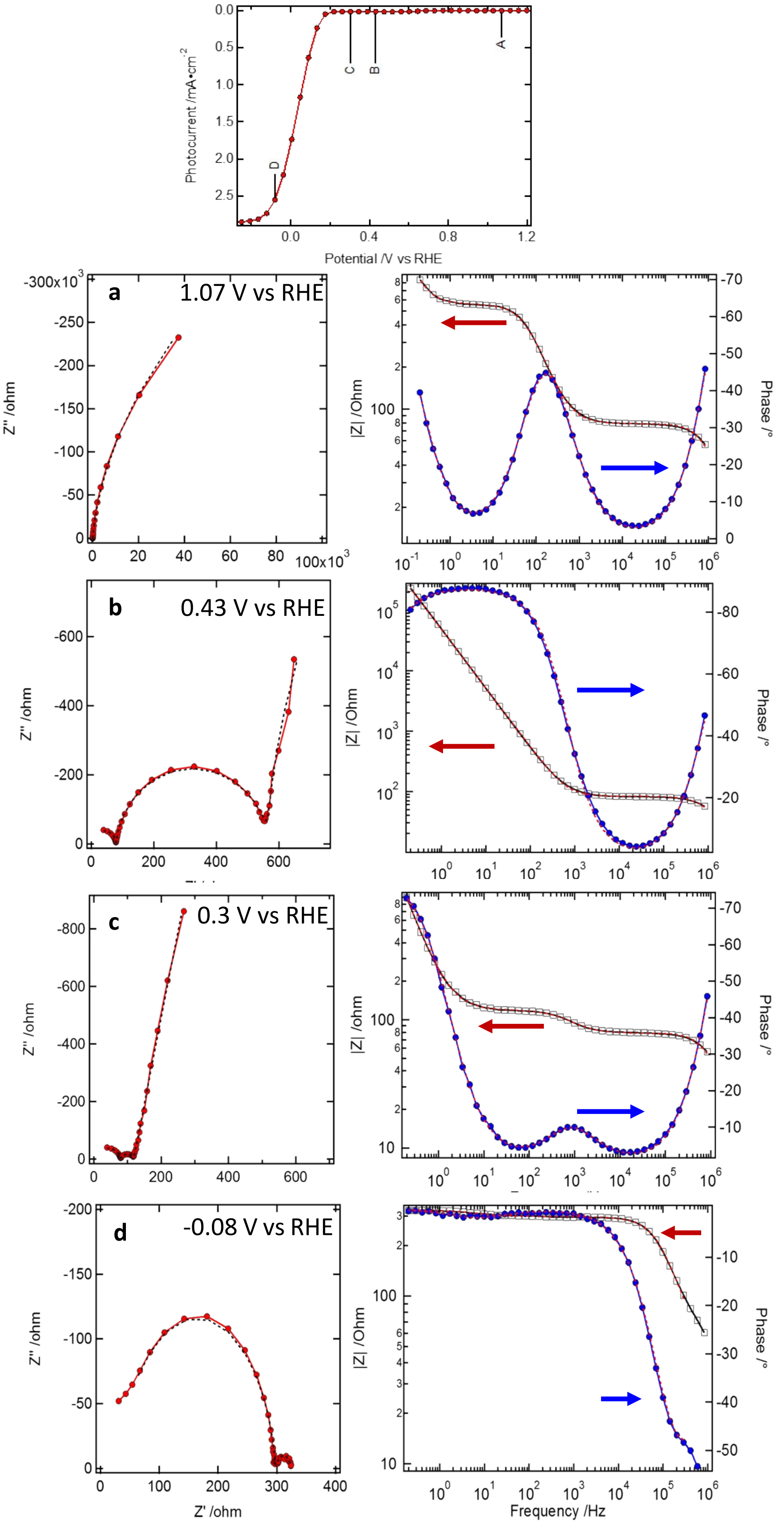

Fig. S 6 Photocurrent (the letters indicate the potentials of the presented EIS data on the JV curve), Nyquist and Bode plots of a silicon device at different bias potentials at 10% sun (solid: EIS data; dotted: fit).

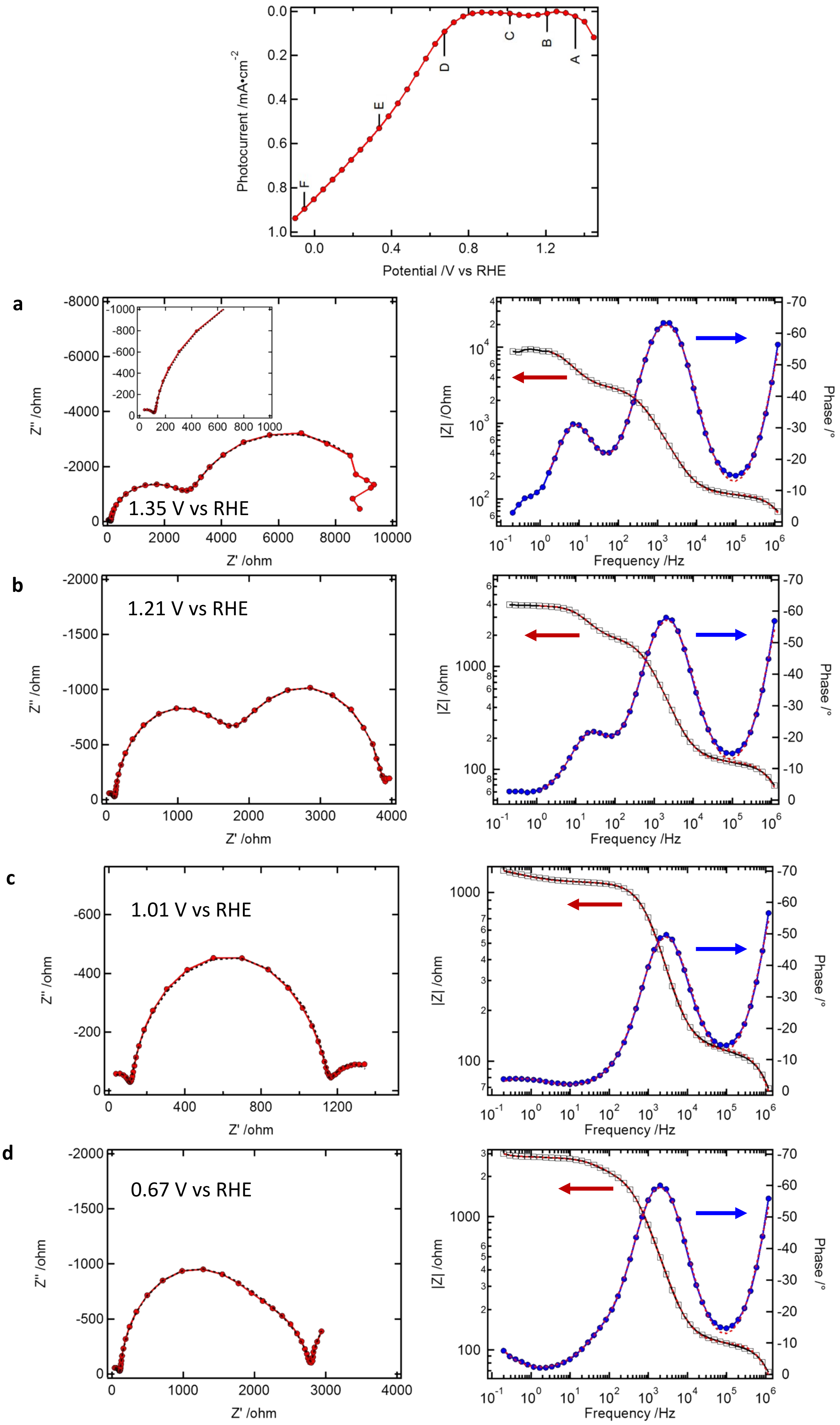

Photocurrent /mA•cm^{-2}
Potential /V vs RHE
A
B
C
D
E
F
a
1.35 V vs RHE
b
1.21 V vs RHE
c
1.01 V vs RHE
d
0.67 V vs RHE
Z'' /ohm
Z' /ohm
|Z| /Ohm
|Z| /ohm
Phase /°
Frequency /Hz

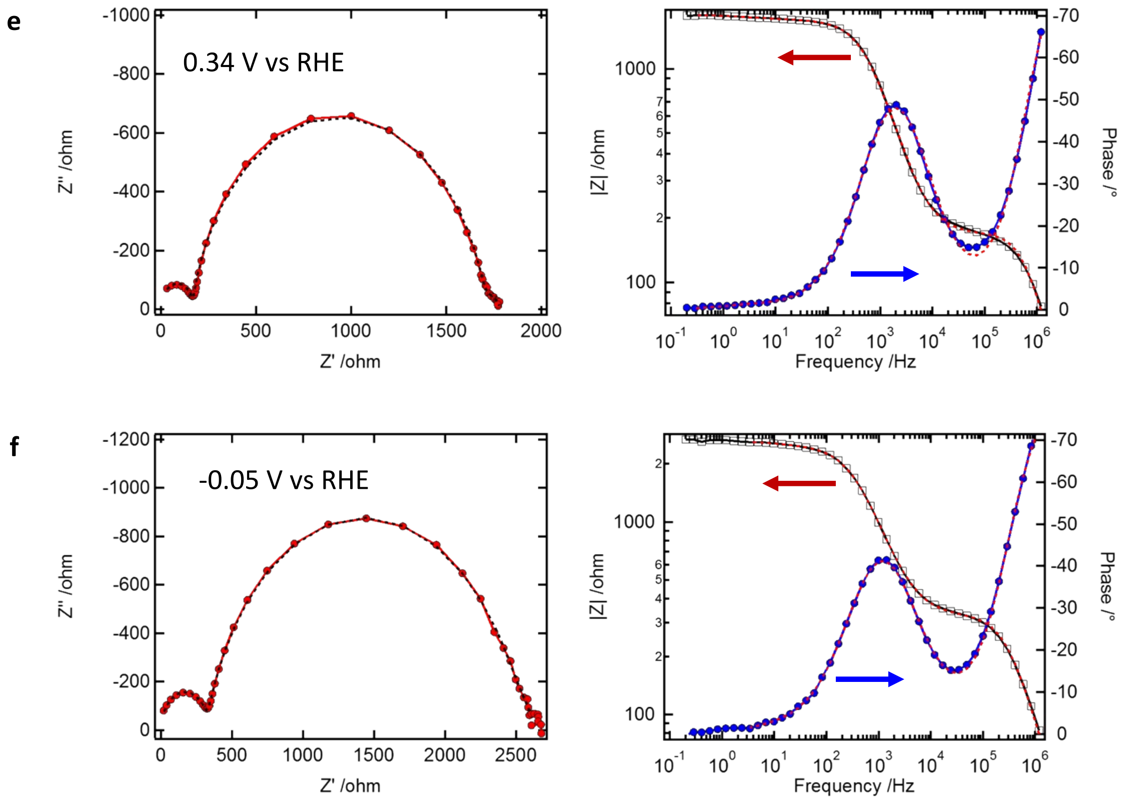

Fig. S 7 Photocurrent (the letters indicate the potentials of the presented EIS data on the JV curve), Nyquist and Bode plots of a Cu_2O device at different bias potentials at 10% sun illumination (solid: EIS data; dotted: fit).

Comparing different devices based on charge transfer resistance (R_{CT})

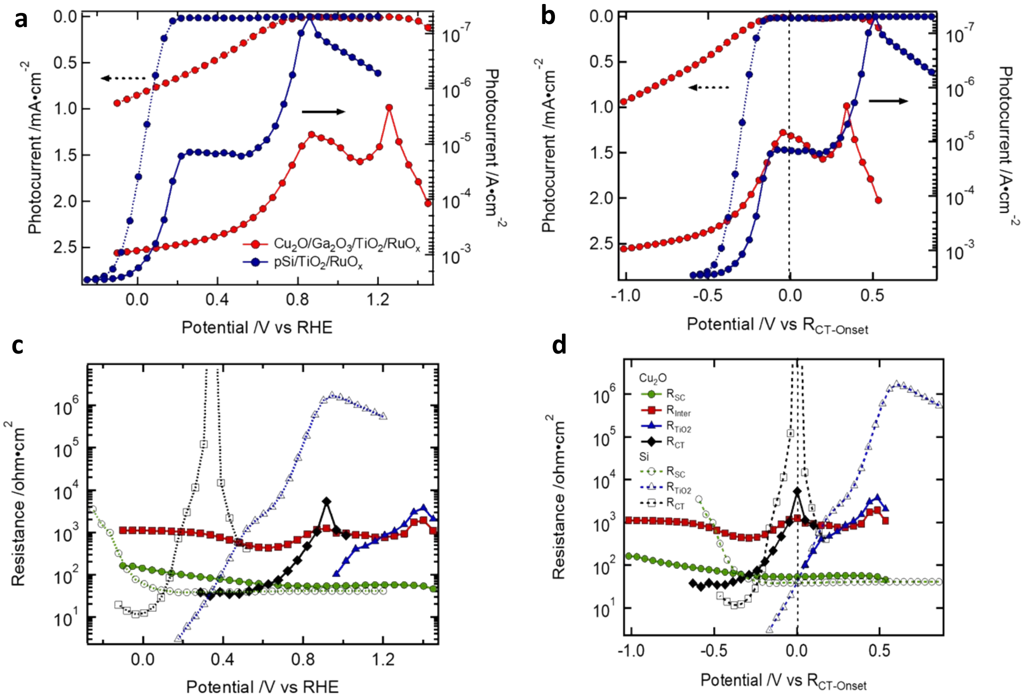

Fig. S 8 (a) JV curves of a silicon (blue) and Cu_2O (red) device from Fig. 2 of the main manuscript; (b) overlay of the two JV curves (shift of the silicon-based devices is 600 mV based on R_{CT} difference between the two different photoabsorber systems); (c) determined resistances for the devices; (d) resistances adjusted to the H_2 onset potential by R_{CT}

To directly compare devices with different V_{oc} due to variation of the protection layer, the interlayer thickness or the absorber material one normally needs to know the exact fermi level position of each single device. On the other hand, the devices have a similar electron fermi level position as soon as the cathodic photocurrent (after the first reduction step of the catalyst) sets in. A more precise determination of this onset-potential can be performed over the R_{CT}. At the onset of potential region III RCT is showing the step decrease showing its capability from this potential on to reduce H_2. Therefore, we can compare the different devices relatively to each other by shifting the data to the same onset potential of potential region III (see also Fig. S 11 thickness comparison of the TiO_2). This way of comparison can even be applied when different absorber materials are used. Fig. S 8a and c show the initial JV curve measurement and the determined resistances for a standard silicon and Cu_2O device. The JV curve of the Cu_2O photocathode and the associated resistances are set to 0 V vs R_{CT} onset determined by the beginning of potential region III. The data of the silicon device is shifted by the difference in R_{CT} of +600 mV (Fig. S 8b and d). Clearly observable is overlap of the R_{TiO2} for the two different photoabsorber systems, confirming the validity of this approach. A similar strategy is applied for DSCs by using the DOS of the TiO_2 particles to adjust the different conduction band positions of the metal oxide due to the different additives inside the electrolyte solution.[18]

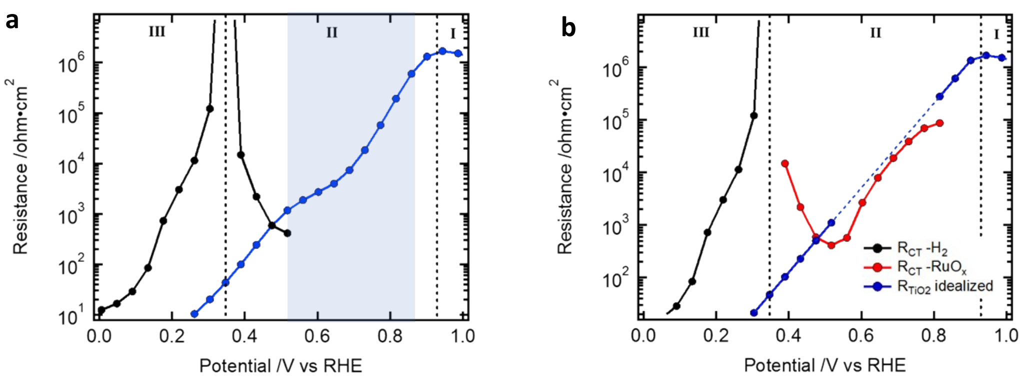

Fig. S 9 Data of Si sample from Fig. 2a in the main manuscript: (a) R_{CT} and R_{TiO2} from the EIS fitting (blue area indicates the potential range used for the exponential fitting procedure in b); (b) exponential fit of R_{TiO2} (blue dotted line) and the residual resistance combined with Rct in potential region II. The residual resistance (R_{CT}-RuO_x) relates to the increased reduction current due to the first reduction step the HEC.

Transient photocurrent decay

An JV curve was recorded prior to each TPC measurement to evaluate the stability of the device. For the actual TPD measurements the bias potential and white light intensity from LEDs were set and then the photocurrent measured. The sample was held under this condition for normally 8s. Then a light pulse of LED (10% of a sun) illuminated the sample for 4 s. The data presented in this manuscript was recorded either with blue (Fig. 5a) or green (Fig. 5b and Fig. S 10) excitation pulses as the excitation by red light mainly probes the bulk of the Cu_2O with the energy of the red pulse being near the absorption edge of the semiconductor. After the light pulse was turned off, the photocurrent was recorded for another 4 s to observe the release of stored charge. The time resolution for detection was 10 ms.

After the transient measurement, a baseline fitting was performed and the white light bias photocurrent subtracted, yielding the bare photocurrent transients (Fig. S 10a). The decay of the photocurrent transients during the light pulse to a steady state current value was normally fitted by a double exponential (see example in Fig. S 10a and b). After the light pulse has been turned off the photocurrent is not directly returning to its initial state but showed the release of stored charge inside the device. Later decay represented normally a single exponential decay.

The time constant and the amount of stored charge of the release process is similar to the slower exponential decay after the excitation pulse (see Tables S3, S4 and S5).

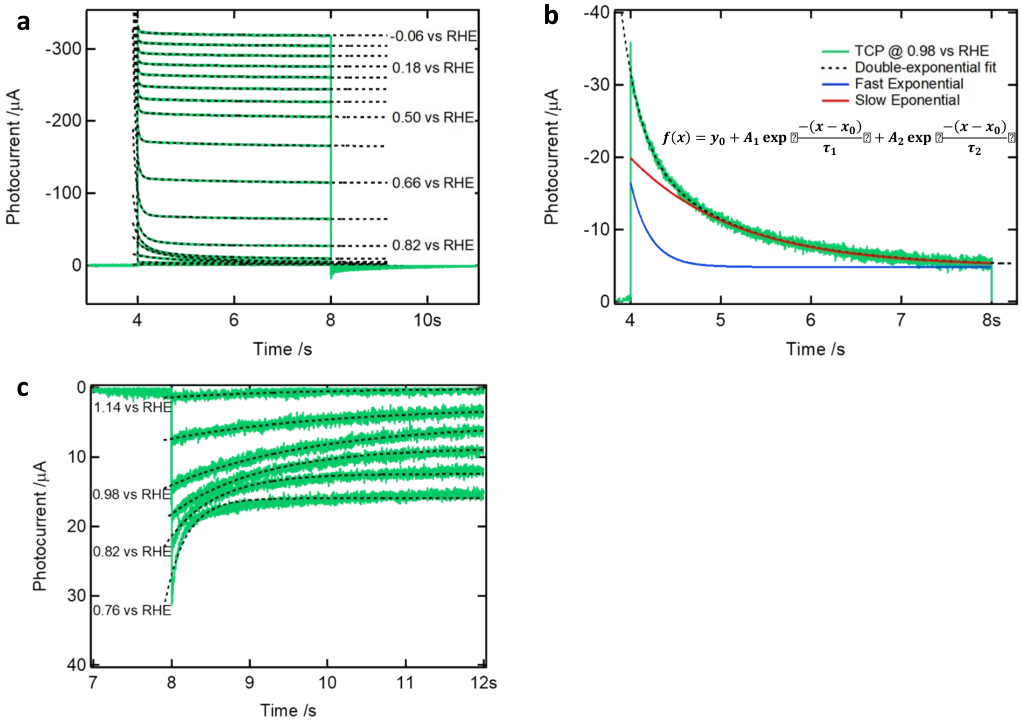

Fig. S 10 (a) Photocurrent decay transients for a standar Cu_2O device at different bias potentials but silimar pulse intensity (10% white light bias, light pulse of 10% sun of 530 nm; green: PC transient, black: double exponential fit, potential steps: 80 mV); (b) Double exponential fit of a transient at 960 mV vs RHE and the two exponentials (inset shows the used fitting function); (c) photocurrent decay (shifted by 3μA cm^{-2} each for better comparison) after the light pulse has been turned of showing the release of stored charge (green: PC transient, black: mono exponential fit).

Tab. S 3 Data from the double exponential fit of the photocurrent transient in Fig. S10 and Fig. 5 for a standard Cu_2O device (with A_1 and τ_1 for the fast component and A_2 and τ_2 for the slow component). At the applied potentials 1.3 and 1.22 vs RHE a mono exponential fit has been used.

Potential V vs RHE	**y_0 /A**	**A_1 /A**	**τ_1 /s**	**A_2 /A**	**τ_2 /s**
1.3	-1.06e-06 (±3.21e-08)			-7.06e-08 (±2.82e-08)	1.54 (±1.96)
1.22	-1.27e-06 (±4.75e-08)			-5.95e-08 (±3.89e-08)	1.94 (±3.61)
1.14	-2.23e-06 (±4.7e-08)	-5.50e-06 (±3.16e-07)	0.00302 (±0.000506)	-2.22e-06 (±3.96e-08)	1.94 (±0.0995)
1.06	-2.92e-06 (±1.08e-07)	-3.44e-06 (±1.99e-07)	0.29163 (±0.0211)	-8.14e-06 (±1.28e-07)	1.81 (±0.0893)
0.98	-4.88e-06 (±3.65e-08)	-1.17e-05 (±1.59e-07)	0.20155 (±0.004021)	-1.54e-05 (±1.46e-07)	1.15 (±0.016)
0.9	-9.52e-06 (±2.52e-08)	-1.94e-05 (±1.22e-07)	0.16454 (±0.001732)	-1.33e-05 (±1.13e-07)	1.02 (±0.0122)
0.82	-2.72e-05 (±1.65e-08)	-2.49e-05 (±1.12e-07)	0.11047 (±0.000945)	-8.99e-06 (±9.93e-08)	0.79 (±0.011)
0.74	-6.41e-05 (±4.62e-08)	-3.21e-05 (±1.05e-07)	0.07505 (±0.000459)	-5.34e-06 (±3.69e-08)	1.57 (±0.0421)
0.66	-0.000114 (±7.5e-08)	-3.02e-05 (±1.28e-07)	0.04973 (±0.000359)	-6.75e-06 (±5.52e-08)	2.10 (±0.0546)
0.58	-0.000165 (±7.96e-08)	-2.20e-05 (±1.47e-07)	0.03924 (±0.000431)	-7.06e-06 (±6.06e-08)	2.16 (±0.0551)
0.5	-0.000205 (±7.65e-08)	-1.57e-05 (±1.9e-07)	0.03064 (±0.000598)	-6.45e-06 (±5.84e-08)	1.99 (±0.0561)
0.42	-0.000226 (±6.51e-08)	-1.36e-05 (±2.17e-07)	0.02765 (±0.000703)	-5.07e-06 (±5.04e-08)	1.74 (±0.0587)
0.34	-0.000244 (±6.45e-08)	-1.10e-05 (±2.11e-07)	0.02955 (±0.000914)	-4.68e-06 (±4.99e-08)	1.72 (±0.063)
0.26	-0.000260 (±5.89e-08)	-1.08e-05 (±2.24e-07)	0.02672 (±0.00089)	-4.35e-06 (±4.7e-08)	1.63 0.0611)
0.18	-0.000275 (±5.4e-08)	-9.70e-06 (±2.2e-07)	0.02872 (±0.00105)	-4.36e-06 (±4.5e-08)	1.53 (±0.0555)
0.1	-0.000290 (±4.87e-08)	-9.82e-06 (±2.35e-07)	0.02617 (±0.001)	-4.20e-06 (±4.4e-08)	1.43 (±0.0511)
0.02	-0.000304 (±4.42e-08)	-9.41e-06 2.54e-07)	0.02484 (±0.00108)	-4.30e-06 (±4.56e-08)	1.30 (±0.0447)
-0.06	-0.000318 (±4.64e-08)	-9.45e-06 (±2.53e-07)	0.02552 (±0.0011)	-4.51e-06 (±4.62e-08)	1.33 (±0.045)
-0.14	-0.000333 (±4.84e-08)	-8.85e-06 (±2.46e-07)	0.02950 (±0.00134)	-4.45e-06 (±4.86e-08)	1.33 (±0.0479)
-0.22	-0.000348 (±5.03e-08)	-1.02e-05 (±2.91e-07)	0.02236 (±0.00102)	-4.74e-06 (±4.95e-08)	1.34 (±0.0461)

Tab. S 4 Data from the mono exponential exponential fit of the release of charge after the light pulse is turned off for a standard Cu_2O *device (Fig. S10 and Fig. 5b).*

Potential /V vs RHE	**y_0 /A**	**A_1 /A**	**τ_1 /s**
1.3	1.52e-08 (±5.39e-09)	6.12e-08 (±3.96e-07)	1.53 (±0.56)
1.22	-6.67e-09 (±1.83e-08)	1.30e-07 (±2.64e-08)	1.02 (±0.559)
1.14	6.36e-08 (±4.29e-08)	1.30e-06 (±3.52e-08)	1.84 (±0.146)
1.06	-2.06e-07 (±6.5e-08)	4.57e-06 (±5.37e-08)	2.12 (±0.0661)
0.98	-8.81e-07 (±5.22e-08)	8.93e-06 (±4.28e-08)	1.86 (±0.0261)
0.9	1.66e-08 (±2.28e-08)	9.06e-06 (±2.82e-08)	1.13 (±0.0101)
0.82	4.85e-07 (±1.3e-08)	9.06e-06 (±4.21e-08)	0.58 (±0.00504)
0.74	1.00e-06 (±1.27e-08)	1.15e-05 (±8.39e-08)	0.25 (±0.00284)
0.66	6.19e-07 (±1.36e-08)	1.19e-05 (±1.19e-07)	0.16 (±0.00244)
0.58	8.05e-07 (±1.3e-08)	8.40e-06 (±1.1e-07)	0.17 (±0.00337)
0.5	8.57e-07 (±1.28e-08)	4.66e-06 (±7.28e-08)	0.31 (±0.00772)
0.42	5.89e-07 (±1.3e-08)	3.54e-06 (±5.82e-08)	0.42 (±0.0116)
0.34	5.47e-07 (±1.35e-08)	3.08e-06 (±5.91e-08)	0.43 (±0.0139)
0.26	4.89e-07 (±1.47e-08)	2.82e-06 (±5.29e-08)	0.53 (±0.0178)
0.18	4.95e-07 (±1.45e-08)	2.71e-06 (±5.21e-08)	0.53 (±0.0183)
0.1	5.11e-07 (±1.38e-08)	2.86e-06 (±5.64e-08)	0.46 (±0.0157)
0.02	4.07e-07 (±1.7e-08)	2.71e-06 (±5.29e-08)	0.60 (±0.0223)
-0.06	4.58e-07 (±1.48e-08)	2.71e-06 (±5.25e-08)	0.53 (±0.0187)
-0.14	5.27e-07 (±1.65e-08)	2.87e-06 (±5.48e-08)	0.57 (±0.02)
-0.22	4.75e-07 (±1.83e-08)	2.86e-06 (±5.35e-08)	0.63 (±0.0229)

Tab. S 5 Stored and released charge from the fitting data in Table S3 and 4 of the Cu_2O sample in Fig. 5b.

Potential /V vs RHE	**Integrated stored charge (slow exponent) /C cm^{-2}**	**Integrated released charge /C cm^{-2}**
1.3	2.51E-07	8.66e-08
1.22	2.52E-07	1.30e-07
1.14	9.77E-06	3.67e-06
1.06	3.38E-05	1.30e-05
0.98	4.31E-05	2.52e-05
0.9	3.38E-05	2.17e-05
0.82	1.80E-05	1.31e-05
0.74	2.01E-05	7.28e-06
0.66	3.12E-05	4.87e-06
0.58	3.32E-05	3.64e-06
0.5	2.93E-05	3.66e-06
0.42	2.08E-05	3.74e-06
0.34	1.88E-05	3.33e-06
0.26	1.70E-05	3.72e-06
0.18	1.59E-05	3.58e-06
0.1	1.47E-05	3.32e-06
0.02	1.38E-05	4.03e-06
-0.06	1.48E-05	3.61e-06
-0.14	1.47E-05	4.04e-06
-0.22	1.57E-05	4.46e-06

Thickness variation of the TiO_2 layer

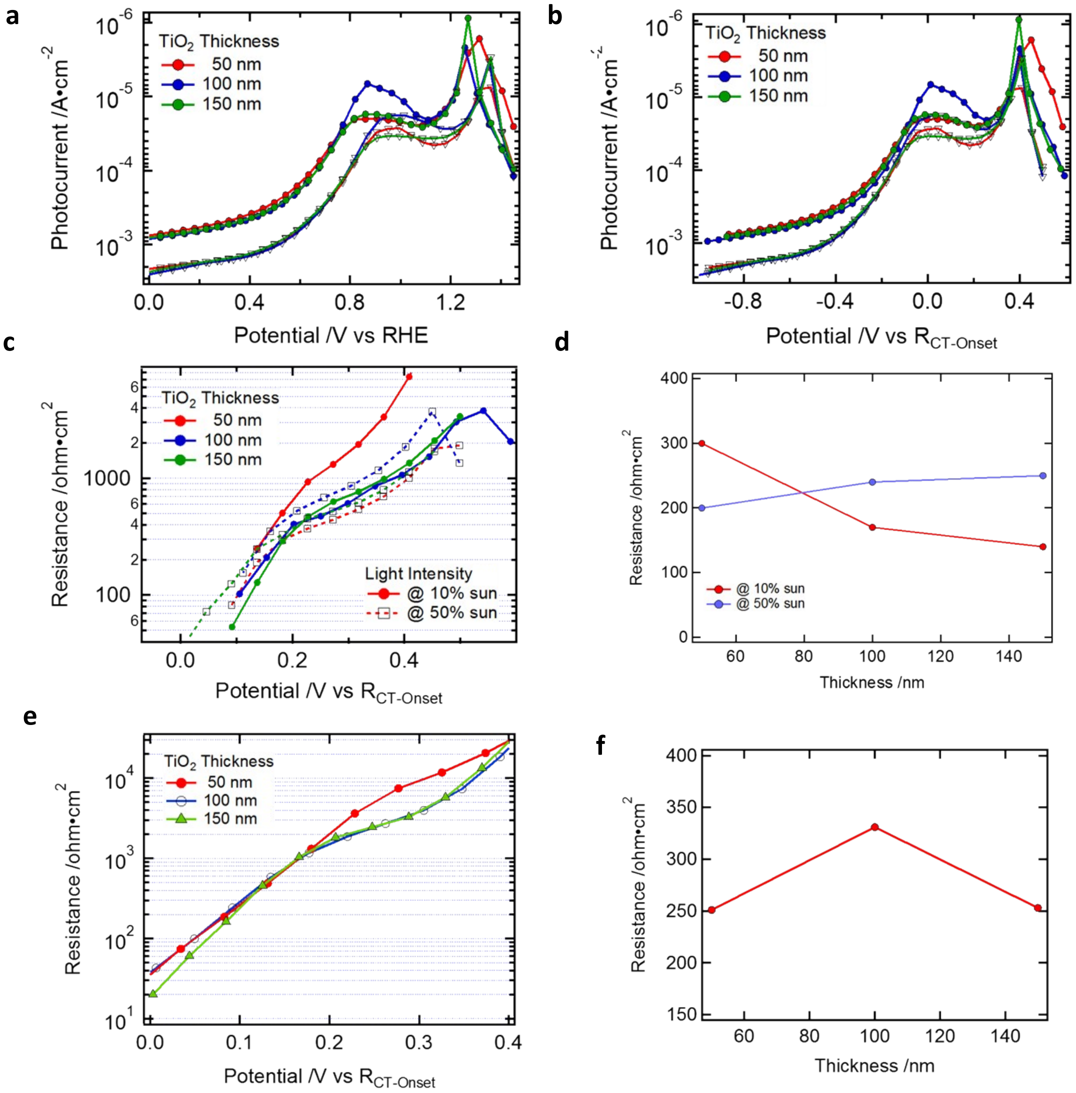

Fig. S 11 (a) to (d): Cu_2O-based devices with different ALD TiO_2 layer thicknesses: (a) JV curve at 10 and 50% of a sun; (b) JV curves shifted by adjusting to R_{CT}; (c) R_{TiO2} from the different devices adjusted by R_{CT}; (d) R_{TiO2} for the different thicknesses at +0.155 V vs R_{CT} onset potential. (e) R_{TiO2} of silicon-based devices at 10% sun with different ALD TiO_2 layer thicknesses adjusted by R_{CT}; (f) R_{TiO2} for the different thicknesses at +0.1 V vs R_{CT} onsetpotential.

Series resistance of the JV curve and R_{Inter}

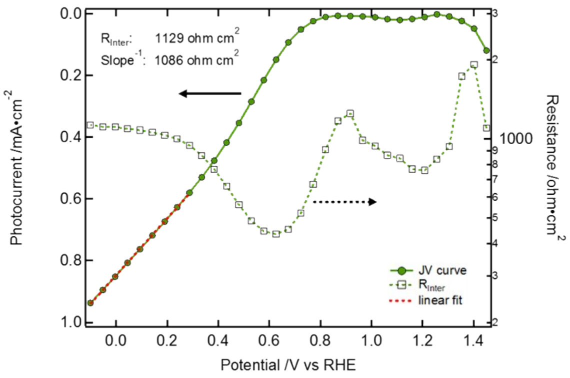

Fig. S 12 JV curve and R_{Inter} of a Cu_2O standard device. The slope of the linear fit of the JV curve in the potential region -100 mV to 300 mV vs RHE yields the series resistance of the device. R_{Inter} is nearly constant in this potential region and shows a similar value as the series resistance determined from the JV curve.

Composition of R_{Inter} out of R_{Ga} and $R_{surface}$

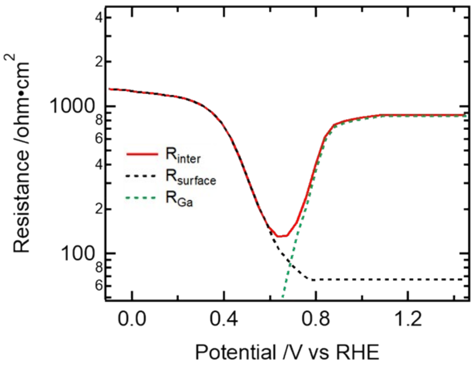

Fig. S 13 R_{inter} composed of R_{Ga} and $R_{surface}$

Charge transfer at the Cu_2O surface

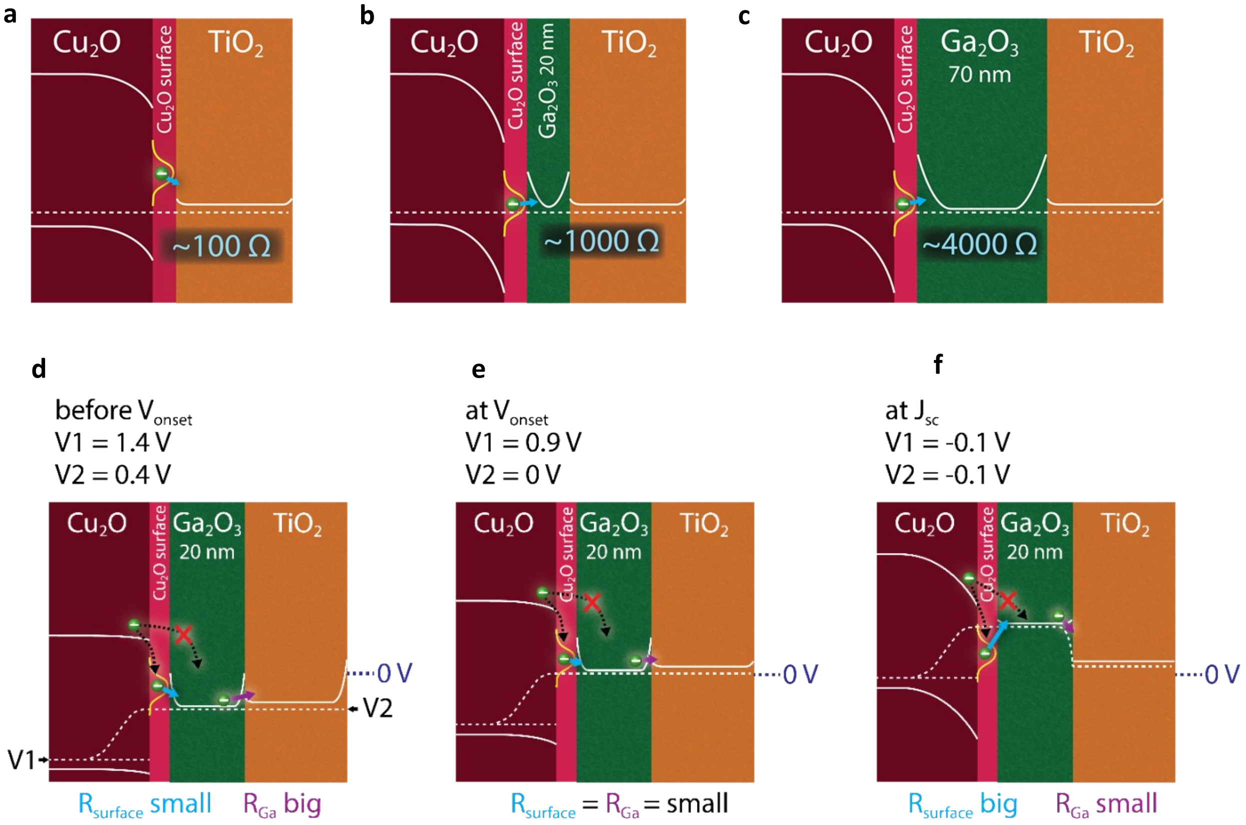

Fig. S 14 (a), (b) and (c) describe the relation of built-in voltage and the resistance $R_{Surface}$ for devices without ALD Ga_2O_3 layer, with 20 nm and with 70 nm ALD Ga_2O_3; (d), (e) and (f) describe the relation between R_{Ga} and $R_{Surface}$ at different bias potentials for a standard Cu_2O photocathode (before H_2 evolution onset potential (d), at the onset of H_2 evolution with the electron quasi Fermi level at 0 V vs RHE (e) and at more negative potentials then the H_2 evolution onset potential (f)).

Pristine and etched Cu_2O surface in complete devices with Ga_2O_3 buffer layer

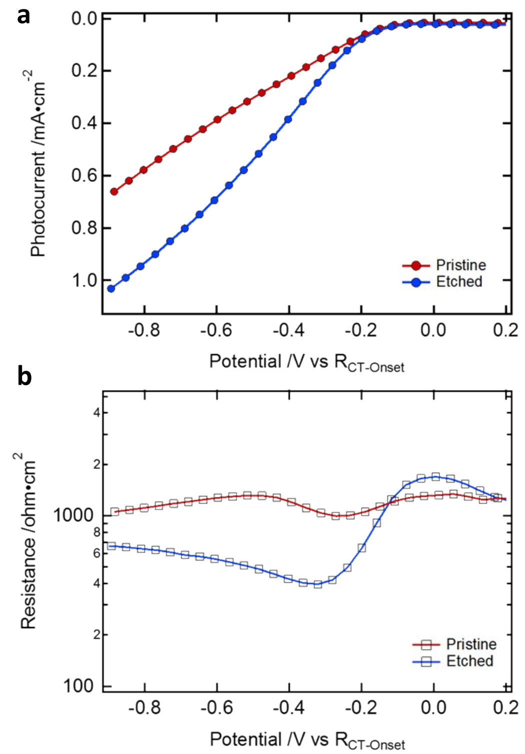

Fig. S 15 (a) JV curves of a pristine and an etched Cu_2O-based standard device at 10% sun; (b) R_{Inter} of the devices presented in (a).

References

1 T. Minami, Y. Nishi and T. Miyata, *Appl. Phys Express*, 2016, **9**, 52301.

2 Tadatsugu Minami and Yuki Nishi and Toshihiro Miyata and Jun-ichi Nomoto, *Appl. Phys Express*, 2011, **4**, 62301.

3 W. Niu, T. Moehl, W. Cui, R. Wick-Joliat, L. Zhu and S. D. Tilley, *Adv. Energy Mater.*, 2018, **8**, 1702323.

4 T. Moehl, J. Suh, L. Sévery, R. Wick-Joliat and S. D. Tilley, *ACS Appl. Mater. Interfaces*, 2017, **9**, 43614.

5 S. D. Tilley, M. Schreier, J. Azevedo, M. Stefik and M. Graetzel, *Adv. Funct. Mater.*, 2014, **24**, 303.

6 F. Biccari, University of Rome, 2009.

7 W. Cui, W. Niu, R. Wick-Joliat, T. Moehl and S. D. Tilley, *Chem. Sci.*, 2018, **9**, 6062.

8 S. J. Calero, P. Ortiz, A. F. Oñate and M. T. Cortés, *Int. J. Hydrogen Energy*, 2016, **41**, 4922.

9 Y.-S. Kim, S. Kriegel, K. D. Harris, C. Costentin, B. Limoges and V. Balland, *J. Phys. Chem. C*, 2017, **121**, 10325.

10 R. L. Anderson, *IBM J. Res. Dev.*, 1960, **4**, 283.

11 S. J. Pearton, J. Yang, P. H. Cary, F. Ren, J. Kim, M. J. Tadjer and M. A. Mastro, *Appl. Phys. Rev.*, 2018, **5**, 11301.

12 E. Pastor, F. Le Formal, M. T. Mayer, S. D. Tilley, L. Francàs, C. A. Mesa, M. Grätzel and J. R. Durrant, *Nat. Commun.*, 2017, **8**, 14280.

13 K. Doblhofer, M. Metikoš, Z. Ogumi and H. Gerischer, *Berichte der Bunsengesellschaft für physikalische Chemie*, 1978, **82**, 1046.

14 J. Juodkazytė, R. Vilkauskaitė, B. Šebeka and K. Juodkazis, *Transactions of the IMF*, 2007, **85**, 194.

15 L. D. Burke and N. S. Naser, *J. Appl. Electrochem.*, 2005, **35**, 931.

16 Y. Sugawara, A. P. Yadav, A. Nishikata and T. Tsuru, *J. Electrochem. Soc.*, 2008, **155**, B897.

17 E. Watanabe, H. Ushiyama, K. Yamashita, Y. Morikawa, D. Asakura, M. Okubo and A. Yamada, *J. Phys. Chem. C*, 2017, **121**, 18975.

18 J.-H. Yum, E. Baranoff, F. Kessler, T. Moehl, S. Ahmad, T. Bessho, A. Marchioro, E. Ghadiri, J.-E. Moser, C. Yi, M. K. Nazeeruddin and M. Grätzel, *Nat. Commun.*, 2012, **3**, 631.